A&A 559, A111 (2013)
DOI: 10.1051/0004-6361/201321616

Astronomy & Astrophysics

An interferometric study of the post-AGB binary 89 Herculis

I. Spatially resolving the continuum circumstellar environment at optical and near-IR wavelengths with the VLTI, NPOI, IOTA, PTI, and the CHARA Array⋆,⋆⋆,⋆⋆⋆

M. Hillen[1], T. Verhoelst[1,2], H. Van Winckel[1], O. Chesneau[3], C. A. Hummel[4], J. D. Monnier[5], C. Farrington[6], C. Tycner[7], D. Mourard[3], T. ten Brummelaar[6], D. P. K. Banerjee[8], and R. T. Zavala[9]

[1] Instituut voor Sterrenkunde (IvS), KU Leuven, Celestijnenlaan 200D, 3001 Leuven, Belgium
e-mail: Michel.Hillen@ster.kuleuven.be
[2] Belgian Institute for Space Aeronomy, 1180 Brussels, Belgium
[3] Laboratoire Lagrange, UMR7293, Univ. Nice Sophia-Antipolis, CNRS, Observatoire de la Côte d'Azur, 06300 Nice, France
[4] European Southern Observatory, Karl-Schwarzschild-Str. 2, 85748 Garching, Germany
[5] University of Michigan, 941 Dennison Building, 500 Church Street, Ann Arbor, MI 48109-1090, USA
[6] The CHARA Array of Georgia State University, Mt. Wilson Observatory, Mt. Wilson, CA 91023, USA
[7] Department of Physics, Central Michigan University, Mt. Pleasant, MI 48859, USA
[8] Physical Research Laboratory, Navrangpura, 380009 Ahmedabad, India
[9] US Naval Observatory, Flagstaff Station, 10391 W. Naval Obs. Rd., Flagstaff, AZ 86001, USA

Received 1 April 2013 / Accepted 25 July 2013

ABSTRACT

Context. Binary post-asymptotic giant branch (post-AGB) stars are interesting laboratories to study both the evolution of binaries as well as the structure of circumstellar disks.
Aims. A multiwavelength high angular resolution study of the prototypical object 89 Herculis is performed with the aim of identifying and locating the different emission components seen in the spectral energy distribution.
Methods. A large interferometric data set, collected over the past decade and covering optical and near-infrared wavelengths, is analyzed in combination with the spectral energy distribution and flux-calibrated optical spectra. In this first paper only simple geometric models are applied to fit the interferometric data. Combining the interferometric constraints with the photometry and the optical spectra, we re-assess the energy budget of the post-AGB star and its circumstellar environment.
Results. We report the first (direct) detection of a large (35–40%) optical circumstellar flux contribution and spatially resolve its emission region. Given this large amount of reprocessed and/or redistributed optical light, the fitted size of the emission region is rather compact and fits with(in) the inner rim of the circumbinary dust disk. This rim dominates our K band data through thermal emission and is rather compact, emitting significantly already at a radius of twice the orbital separation. We interpret the circumstellar optical flux as due to a scattering process, with the scatterers located in the extremely puffed-up inner rim of the disk and possibly also in a bipolar outflow seen pole-on. A non-local thermodynamic equilibrium gaseous origin in an inner disk cannot be excluded but is considered highly unlikely.
Conclusions. This direct detection of a significant amount of circumbinary light at optical wavelengths poses several significant questions regarding our understanding of both post-AGB binaries and the physics in their circumbinary disks. Although the identification of the source of emission/scattering remains inconclusive without further study on this and similar objects, the implications are manifold.

Key words. stars: AGB and post-AGB – circumstellar matter – binaries: general – techniques: interferometric – scattering – ISM: jets and outflows

1. Introduction

Waters et al. (1993) defined 89 Her as the prototype of a new class of post-asymptotic giant branch (post-AGB) binaries surrounded by circumbinary dust disks. Subsequent studies (de Ruyter et al. 2006; van Winckel et al. 2009) found a link between binarity and the presence of both hot and cool circumstellar material for many high galactic latitude supergiants. The infrared excesses are very similar to those observed for young stellar objects (YSOs) and strongly suggest a disk-like origin in all these sources (Gielen et al. 2011, and references therein).

The orbital elements of post-AGB binaries show their companion stars to be most likely on the main sequence and to have separations of ∼1 AU (van Winckel et al. 2009), which are too small to harbor an AGB star. Moreover, most post-AGB binaries are still O-rich (Gielen et al. 2011), which suggests that their

⋆ Based on observations made with ESO Telescopes at the La Silla Paranal Observatory under program ID 079.D-0013 and 089.D-0576.
⋆⋆ Figures 2, 4, 6, 7, 9, 10, and Table 5 are available in electronic form at http://www.aanda.org
⋆⋆⋆ FITS files of the calibrated visibilities are only available at the CDS via anonymous ftp to cdsarc.u-strasbg.fr (130.79.128.5) or via http://cdsarc.u-strasbg.fr/viz-bin/qcat?J/A+A/559/A111

evolution was cut short during a very short-lived phase. In this phase, a significant part of the primary's mass is expelled into a circumbinary orbit while avoiding a common envelope situation (see, e.g., Mastrodemos & Morris 1998; van Winckel 2003; Frankowski & Jorissen 2007). Due to the large and badly constrained distances, luminosities are not well known; this hampers progress in connecting them to other classes of the binary zoo. But disk formation is found to be a mainstream process around evolved stars, as was recently found in the Large Magellanic Cloud (LMC; van Aarle et al. 2011).

With optical interferometers now online, it is possible to resolve the prevailing circumstellar geometries for stars all over the Hertzsprung-Russell diagram, from optical to mid-IR wavelengths. For YSOs this has led to the discovery of an empirical size-luminosity relation (Millan-Gabet et al. 2001; Monnier & Millan-Gabet 2002), which in turn has led to the current paradigm (Dullemond & Monnier 2010) of a passive dusty disk with an optically thin cavity and the inner radius set by the dust sublimation distance. The appearance and evolution of YSOs and binary post-AGB disks are likely dictated by the same processes, but differences in gravity, luminosity, and evolutionary timescales should lead to different disk evolution. Disks around binary post-AGB stars have been much less the subject of interferometric study. A few objects were investigated (Deroo et al. 2006, 2007) with the MIDI and AMBER instruments on the Very Large Telescope Interferometer (VLTI), providing the final piece of evidence that the IR excess arises from a very compact disk-like geometry. But a detailed analysis of the compact structures remains to be performed.

We present in this paper the first detailed multiwavelength interferometric analysis of the prototypical object 89 Herculis. Bujarrabal et al. (2007) presented some N-band interferometric data in addition to their Plateau de Bure Interferometer CO maps. The latter contained two nebular components, 1) an extended hour-glass-like structure with expansion velocities of 7 km s^{-1}; and 2) the unresolved, smaller than 0.4″, Keplerian disk with a velocity dispersion of only 5 km s^{-1}. They also derived the inclination of the system under the assumption that the symmetry axis of the resolved outflow is perpendicular to the binary orbital plane (Table 1). Attempts to spatially resolve any extended structure at optical and mid-IR wavelengths with the *Hubble* Space Telescope (HST; Siódmiak et al. 2008) and VISIR/VLT (Lagadec et al. 2011) failed to detect any emission at angular scales beyond ~50 and ~300 mas, respectively.

We collected a large set of observations from the VLTI, the Navy Precision Optical Interferometer (NPOI), the Palomar Testbed Interferometer (PTI), the Infrared Optical Telescope Array (IOTA) and the Center for High Angular Resolution Astronomy (CHARA) Array, covering 0.5 to 2.2 μm and with baselines from 15 to 278 m. Here we describe these observations and our simple geometric analysis. With these results, the spectral energy distribution (SED) is then redefined. In Paper II, a detailed radiative transfer modeling will be attempted to reproduce our observables.

2. Observations and data reduction

2.1. Interferometry

A log of all interferometric observations is presented in Table 2. Below we discuss the individual data sets. Figure 1 shows the obtained UV coverage. Figures 2–5 (some only available online) depict the near-IR calibrated visibilities and the IOTA closure phases. The optical visibilities are visible in Figs. 5 and 6.

Table 1. Stellar and binary parameters of 89 Herculis.

Parameter	Value	Error	References
Sp.T.	F2Ibe	–	–
$T_{\rm eff}$ (K)	6550	100	1, 2
$\log g$	0.55	0.25	1, 2
[Fe/H]	–0.5	0.2	1, 2
$P_{\rm orb}$ (d)	288.36	0.71	3
e	0.189	0.074	3
$a_1 \sin i$ (AU)	0.080	0.007	3
f(m) ($M_\odot$)	0.00084	0.00022	3
i(°)	12	3	4
π (mas)	0.76	0.23	5
d (kpc)	1.5	$^{+1.0}_{-0.5}$	5

References. (1) Luck et al. (1990); (2) Kipper (2011); (3) Waters et al. (1993); (4) Bujarrabal et al. (2007); (5) van Leeuwen (2007).

2.1.1. Near-IR

VLTI: the object 89 Herculis was observed with the AMBER instrument (Petrov et al. 2007) on the VLTI using the Auxiliary Telescopes (ATs) in 2007, 2008, and 2012, all in the low-spectral-resolution (R = 30) mode covering the H and K bands with detector integration times (DITs) of 25 and 50 ms and without the use of the fringe tracker FINITO. Because 89 Her is quite northern for the Paranal site, observing conditions were never excellent. In 2007 the observations occurred under good atmospheric conditions, with good seeing (~0.8″) and coherence time (2.5–3.0 ms). In 2008 conditions were a bit worse (~1.0″, 2.5 ms) and in 2012 they were bad (>1.0″, 2 ms, and variable). The data were reduced with *amdlib* v3.0.3, which is provided by the Jean-Marie Mariotti Center (JMMC; Tatulli et al. 2007; Chelli et al. 2009) and calibrated with observations of HD 165524 (Mérand et al. 2005).

The 10% of the best signal-to-noise ratio (S/N) frames were used for visibility amplitude estimation, while 80% of all frames were used to compute the closure phases. The exact values of these thresholds have little influence on the final numbers. A small correction to the wavelength table, in the form of a linear offset of –0.08, –0.08, and –0.07 μm for 2007, 2008, and 2012, respectively, was performed to align the H-K discontinuity correctly. Although the final calibration only used the actual calibrator, we checked the consistency of the calibration and the stability of the transfer function by repeating the calibration with each calibrator observed during that night. The generally small spread from this procedure was added to the final error budget to account for the lack of a second dedicated calibrator measurement in the 2007 and 2008 data set. Although the 2007 and 2008 data were observed at the same spatial frequencies, the visibilities are very different. The difference is larger in H band, but the short-wavelength end of the K band is also affected, showing that it is not just the absolute calibration in H band. The largest effect is observed for the shortest baselines. Based on our careful analysis, and the stability of the transfer function, we cannot find a reason why the visibilities are so different, and so the observed trend might be a real time-variable effect. Nevertheless, we decided not to use the 2007 data in our analysis because they are clearly discrepant from the 2008 data, which in turn are consistent with the 2003 IOTA as well as with the 2012 VLTI and CHARA results.

CHARA: both the CLASSIC and CLIMB beam combiners on the Georgia State University CHARA Array interferometer were

Table 2. Observing log of our interferometric observations.

Date	Mean MJD	Instrument	Stations	Nr. Obs.	$\lambda(\mu m)$	$\delta\lambda$ (μm)	Calibrators[a]
2001 May 8	52 037.5	PTI	NW	8	1.65	0.05	HD 166014, HD 168914
2001 Jun. 6	52 066.4	PTI	NW	5	1.65	0.05	HD 166014, HD 168914
2001 Jun. 23	52 083.3	PTI	NS	7	2.1	0.1	HD 166014, HD 168914
2001 Jul. 2,15	52 098.5	PTI	NW	7	1.65	0.05	HD 166014, HD 168914
2001 Jul. 28	52 118.2	PTI	NW	2	2.1	0.1	HD 166014, HD 168914
2001 Aug. 2, 6, 10, 11, 18	52 132.	PTI	NS	27	1.65	0.05	HD 166014, HD 168914
2003 Jun. 10	52 800.3	PTI	NS	7	1.65	0.05	HD 166014, HD 168914
2003 Jun. 15, 16	52 805.8	IOTA	N35-C10-S15	23	1.65	0.25	HD 166014, HD 168914
2007 Apr. 13	54 203.38	AMBER	E0-G0-H0	1	1.50–2.50	0.03	HD 165524
2008 Mar. 31	54 556.39	AMBER	E0-G0-H0	1	1.50–2.50	0.03	HD 165524
2011 Jun. 8	55 720.5	VEGA	S1-S2	1	0.672	0.015	HD 168914
2011 Aug. 24	55 797.5	VEGA	E1-E2	1	0.672	0.015	HD 168914
2011 Oct. 9	55 844.16	NPOI	AC0-AE0	7	0.56–0.85	0.025	HR6787
2011 Oct. 9	55 844.16	NPOI	AE0-AW0	7	0.56–0.85	0.025	HR6787
2012 May 1	56 048.43	CLASSIC	S1-S2	4	2.13	0.3	HD 162828, HD 163948, HD 164730
2012 May 1	56 048.48	CLASSIC	S1-S2	2	1.65	0.2	HD 161239, HD 164730
2012 Jun. 27	56 105.15	AMBER	A1-C1-D0	1	1.50–2.50	0.03	HD 165524
2012 July 3	56 111.46	CLIMB	S2-E2-W2	1	2.13	0.3	HD 166230
2012 July 4	56 112.41	CLIMB	S1-E2-W2	2	2.13	0.3	HD 166230, HD 168914
2012 July 7	56 115.43	CLIMB	S1-E2-W1	2	1.65	0.2	HD 166230, HD 168914

Notes. [(a)] Calibrator UD diameters (mas): HD 166014 = 0.58 ± 0.03, HD 168914(R) = 0.45 ± 0.03, HD 168914(HK) = 0.46 ± 0.03, HD 165524 = 1.11 ± 0.02 (Mérand et al. 2005), HR6787 = 0.34 ± 0.02, HD 162828 = 0.72 ± 0.05, HD 161239 = 0.62 ± 0.04, HD 163948 = 0.52 ± 0.03, HD 164730 = 0.75 ± 0.05, HD 166230 = 0.41 ± 0.03 .

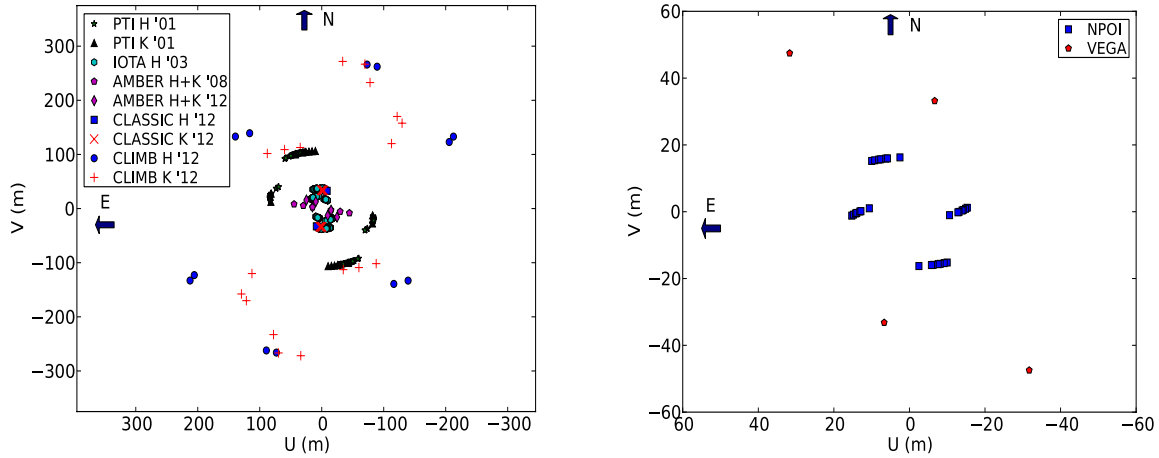

Fig. 1. Baseline coverage of our observations. *Left panel*: the total near-IR UV coverage, *right panel*: total optical UV coverage.

used to conduct observations in the *H* and *K* bands. The CHARA Array, located on Mount Wilson, is a six-telescope Y-shaped interferometric array and contains the longest optical/IR baselines currently in operation (ten Brummelaar et al. 2005). Its 15 baselines, ranging from 34 to 331 m, provide resolutions up to ∼0.5 and ∼0.2 mas at near-IR and optical wavelengths respectively. In May 2012 observations were performed with the sensitive two-beam CLASSIC beam combiner in both *H* and *K* band, using the S1S2 34 m baseline. Three-beam CLIMB observations, in *H* and *K* band, were also obtained during three nights in July 2012 on three different station triplets with baseline lengths from 150 to 278 m. Conditions during all nights were good and stable. Data reduction and calibration were carried out with standard CHARA Array reduction software (ten Brummelaar et al. 2012). Calibrators were selected with the JMMC SearchCal tool (Bonneau et al. 2006). All calibrators are less than 7.5° away from the science target, have a brightness difference of at most 1 mag at the wavelength of observation, and have visibility accuracies better than 7% at the resolution of our observations. The final calibration uncertainties include both the scatter of the data from the repeatability of the measured calibrator visibility amplitude and a term accounting for the calibrator diameter uncertainties. The latter contribution is negligible for the CLASSIC data but becomes important for the long CLIMB baselines.

PTI: we retrieved and calibrated observations from the PTI archive, which was made available by the NASA Exoplanet Science Institute (NExScI)[1]. The PTI was a near-IR interferometer consisting of three 40 cm apertures at fixed separations of 85 to 110 m that were combined pairwise (Colavita et al. 1999). Observations were performed in four and five spectral channels covering the *H* and *K* band, respectively. The data reduction was performed on site (Colavita 1999), leaving only the calibration to be done with the *nbCalib* tool (provided by the NExScI, Boden et al. 1998). 89 Her was observed during 30 nights between 1999

[1] http://nexsci.caltech.edu

and 2003, equally spread over the H and K bands. The NW baseline was used during some nights in 2001, however, all other observations were taken with the NS baseline only. Four of the 30 nights were discarded due to inconsistent estimates of the visibility calibration when different calibration measurements were used. Since all observations at the same physical baseline give the same visibility within their (small) errors and probe the same uv coordinates, we select in the K band one particularly stable night per baseline to avoid too large a weight of the PTI data in the LITpro modeling (Sect. 3). All data are retained in the H band as their number matches that of the IOTA data set. The two calibrators were originally selected using getCal, an SED-fitting routine maintained and distributed by the NExScI. However we fetched their angular diameters (which are well below the resolution limit of PTI) with SearchCal for HD 168914 and from the catalog of van Belle et al. (2008) for HD 166014. Since SearchCal quotes a significantly smaller angular diameter (~30%) for the latter calibrator, we checked and confirmed the value found by van Belle et al. (2008) by fitting Kurucz model atmospheres to archival photometry using the same tools as described in Sect. 4. The final precision of the PTI observations is ~5%, which is typical for PTI and an object of the given brightness.

IOTA: eight and 15 observations of 89 Her were obtained at the IOTA interferometer (Traub et al. 2003) on 2003 June 15 and 16, respectively. This interferometer was located on Mt. Hopkins (AZ) and consisted of three 0.45 m telescopes that were movable about 17 stations along two orthogonal linear arms. Our observations were done at stations N35-C10-S15. They included three simultaneous baselines using the broadband H filter. The light beams from the three telescopes were interfered using the single-mode IONIC3 combiner (Berger et al. 2003). The data reduction was the same as described in previous IOTA papers (e.g., Monnier et al. 2006). Also, closure phases were procured with a precision of 1–3°. The same calibrators were used as for the PTI.

2.1.2. Optical

NPOI: the NPOI was described by Armstrong et al. (1998). Observations of 89 Her were carried out in October 2011, but only in one night were the seeing conditions good enough to allow further analysis of the data. For technical reasons, only two baselines were available, between the astrometric east (AE) and center (AC) station, and between the latter and the west station (AW). Therefore, no closure phase data were recorded. Additional "incoherent" observations away from the fringe packet were recorded for each star in order to determine the visibility bias. As a calibrator, HR 6787 was interleaved with the seven observations of 89 Her. The data reduction followed the steps outlined by Hummel et al. (2003). Based on apparent magnitudes and colors, the calibrator diameter was estimated to be 0.34 mas, implying that it was unresolved by the interferometer. Calibration uncertainties based on the repeatability of the calibrator visibility amplitude ranged from a few percent in the reddest channel (channel 1, 860 nm) up to about 10% in the bluest channel (channel 16, 560 nm).

CHARA: two observations were performed in June and August 2011 with the Visible spEctroGraph And Polarimeter (VEGA instrument, Mourard et al. 2009) integrated within the CHARA Array. VEGA was used to recombine two telescopes, first S1S2 (34 m) and then E1E2 (62 m). The spectrograph is designed to sample the visible band from 0.45 to 0.85 μm, and VEGA is equipped with two photon-counting detectors looking at two different spectral bands. The observations were performed with the medium-resolution setting of $R = 6000$ under average-to-poor seeing conditions ($r_0 \sim 4$–7 cm), with HD 168914 as the calibrator.

The data reduction method is fully described in Mourard et al. (2009) and we only briefly summarize it here. The spectra are extracted using a classical scheme of collapsing the 2D flux in one spectrum, wavelength calibration using a Th-Ar lamp, and normalization of the continuum by polynomial fitting. The raw squared visibilities were estimated by computing the ratio of the high-frequency energy to the low-frequency energy of the averaged spectral density. The same treatment was applied to the calibrators, whose angular diameter was estimated with SearchCal.

The signal was extracted from a band of 15 nm centered around 672.5 nm. Given the limited S/N, it was not possible to extract a useful differential signal over the Hα line.

2.2. Photometry

Photometric measurements with reliable transmission curves and zero points were already analyzed in de Ruyter et al. (2006; i.e., GENEVA, IRAS, JCMT), but we also included AKARI data (Murakami et al. 2007), UV photometry from TD1 (Thompson et al. 1978) and from the ANS satellite (Wesselius et al. 1982), JOHNSON 11-band measurements (Ducati 2002), and Stromgren points from the GCPD (Mermilliod et al. 1997). Also DIRBE photometry (Smith et al. 2004) in the 3.5, 4.9, and 12 μm bands was included, as well as the WISE W4 band (Cutri & et al. 2012). Other bands in the latter systems were excluded because of too large errors or saturation effects. Near-IR JHK photometry of 89 Her was obtained at a mean UT = 19.645 October 2012 with the Mount Abu 1.2 m telescope using the 256×256 HgCdTe NICMOS3 array of the Near-Infrared Imager/Spectrometer, which has a similar spectral response as the 2MASS system. The details of the observing and data reduction techniques are given in Banerjee & Ashok (2002). Calibration was done with the standard star SAO 86043.

2.3. Spectroscopy

Observations of 89 Her were procured with the short (SWS) and long (LWS) wavelength spectrometers onboard ISO. We downloaded from the archive the reduced and calibrated spectrum, which covers 2.5–120 μm. The features in this spectrum were already analyzed by Molster et al. (2002), so we refer to this paper for more information. The absolute calibration of the spectrum agrees very well with the retrieved IRAS, AKARI, DIRBE, and WISE photometry, but flux levels at near-IR wavelengths seem to be slightly overestimated.

A near-IR spectrum was retrieved from the atlas of medium-resolution K band spectra published by Wallace & Hinkle (1997). Despite the limited resolution and S/N, the spectrum shows the CO 2–0 and higher vibrational modes in emission, pointing at the presence of a high column density of hot gas.

89 Her is part of our spectroscopic monitoring program of evolved binaries (see, e.g., Van Winckel et al. 2012; Gorlova et al. 2012) with the HERMES spectrograph ($R = 85\,000$, 3770–9000 Å, Raskin et al. 2011) on the 1.2 m Mercator Telescope at the Roque de los Muchachos Observatory,

Table 3. Observing log of the HERMES spectra that were used to obtain optical spectral slopes.

Date	MJD	Calibrator	V_{cal}	Sp. T.	$T_{exp,cal}$ (s)	$T_{exp,sci}$ (s)	$Airmass_{cal}$	$Airmass_{sci}$
2011 Aug. 05	55 779.38	HD 152614	4.38	B8V	330	120	1.06	1.01
2011 Sep. 21	55 826.35	HD 185395	4.48	F4V	360	150	1.09	1.07
2011 Oct. 09	55 844.32	HD 184006	3.77	A5V	190	120	1.09	1.11

La Palma. A detailed account of this large set of high-resolution spectra will be presented elsewhere. Here we simply use some of them, i.e., those with good S/N and close in time to the interferometric observations and to suitable calibrator observations (Table 3), as an independent constraint on the optical continuum spectral slope. The latter can be calibrated well thanks to the high stability of the HERMES instrument, which is monitored by measuring standard stars each night. We use these standard star measurements for our a posteriori spectral shape calibration. The intrinsic calibrator spectrum was determined by fitting a reddened Kurucz model atmosphere (Kurucz 1993) to high-quality archival photometry (obtained from the same catalogs as described above, see Sect. 4 for a description of the fitting procedures). After convolution to a lower resolution wavelength grid, the intrinsic calibrator spectrum as well as the measured counts of both science and calibrator spectrum are normalized at 7400 Å, where the HERMES throughput is maximal. The calibrated result is then the product of the intrinsic calibrator spectral shape with the measured science one, divided by the measured calibrator spectral shape. The scatter between calibrations with different calibrators and exposures is small.

3. A geometric analysis

Using the efficient LITpro software (Tallon-Bosc et al. 2008) provided by the JMMC, we fit and analyze in this section the near-IR and optical interferometric data with simple geometric models to deduce sizes and flux ratios of the different physical components. We start with the near-IR because of our experience with similar data on other disk sources and then continue with the unexplored optical regime. Given the nondetection of large-scale nebulosity at optical and mid-IR wavelengths, there is no need to take into account potential field-of-view (FOV) issues.

3.1. A ring in the near-IR

We first describe the general fitting process and then compare the results for the H and K bands. Our prime interest in this study is to constrain the broadband morphology of the object. We choose not to use the full spectral capabilities of AMBER (which even in the low resolution mode are significantly better than for the other instruments) and PTI. For simplicity, we select the wavelength channels that are closest to the central wavelengths of the CLIMB, CLASSIC, and IONIC3 broad passbands. Although a small bias might be introduced, the smooth and monotonic wavelength dependence of the visibility validates our approach.

Monnier & Millan-Gabet (2002) argued that fitting near-IR visibilities of protoplanetary disks with a uniform ring model is well justified: in the standard model of a passive disk, the near-IR emission is dominated by the hottest dust at the sublimation radius. This simple model works well if the inclination is small and if the region between the central star and the inner rim is optically thin. The first condition is certainly fulfilled for 89 Her (with $i \sim 10$–$15°$), so we use such a pole-on star+ring model. In Sects. 3.2 and 3.4, we discuss the properties of the central binary and how it affects our observations in more detail; here we assume a single star at the center of the ring. Our model parameters are the angular diameter of the post-AGB star $\theta_\star$, the inner diameter of the ring θ_{in}, the width of the ring $\Delta(\theta_{in}/2)$, and the flux ratio of the two components $f_\star = F_\star/F_{tot}$ and $1 - f_\star = F_{ring}/F_{tot}$. The visibility is computed as $V = f_\star V_\star + (1 - f_\star)V_{ring}$.

Table 4. Parameter space for a star+ring model searched with LITpro, and the final best-fit values.

Parameter	Range	Best H	Best K	Best optical
$F_\star/F_{tot}$	(0.0, 1.0)	0.56 ± 0.05	0.28 ± 0.05	0.65 ± 0.07
F_{ring}/F_{tot}	(0.0,1.0)	0.44 ± 0.05	0.72 ± 0.05	0.35 ± 0.07
$\theta_\star$ [a] (mas)	(0.2, 0.7)	0.45±0.15	0.435[b]	0.435[b]
θ_{in} [a,c]	(1.0, 30.0)	2.5 ± 1.0	4.1 ± 0.4	3 ± 2
$\Delta(\theta/2)$ [a,c]	(1.0, 15.0)	4.5 ± 1.0	4.0 ± 0.2	3 ± 2
$\chi^2_r \pm \sigma$ [d]	–	11.8 ± 0.1	3.8 ± 0.3	2.1 ± 0.1

Notes. [(a)] θ denotes diameter (mas), so $\Delta(\theta/2)$ is the width of the ring as the difference between its outer and inner radius. [(b)] Data impose no constraint, so value fixed from SED fit. [(c)] A strong correlation exists between these parameters, so the given errors reflect the range of good χ^2_r. We refer to the χ^2_r maps for a better estimate of the confidence interval. [(d)] This is the final χ^2_r obtained by fitting all parameters, as opposed to the χ^2_r maps where only the shown parameters are left free. So the number of degrees of freedom is slightly different in both cases.

Table 4 lists the parameter space that was examined. The good uv coverage allows the size and flux contribution of the uniform ring to be constrained, independently of any assumptions or spectral fitting. A first estimate of the flux ratio was determined from the height of the visibility plateau at the highest spatial frequencies, where $V_{ring} \sim 0$ and $V_\star \sim 1$. The K band spatial resolution is insufficient to be sensitive to $\theta_\star$. Stellar diameters >0.6 mas only fit the H band data when combined with large stellar flux contributions and specific ring sizes (so that its higher lobes compensate the visibility drop due to the large $\theta_\star$) and are assumed to be local minima. The H band data are most compatible with $\theta_\star = 0.45 \pm 0.15$ mas, which is also found from SED fitting in Sect. 4, and we fix this value in what follows. The global χ^2_r minimum was found through a Levenberg-Marquardt optimization, starting from the best minimum found in the χ^2_r maps of the ring parameters for a range of flux ratios.

The best-fit values are listed in Table 4. The χ^2_r maps for the best-fit flux ratios are shown in Fig. 8 and the best-fit model visibility curves in Figs. 3 and 4 (available online). Their left panels also contain the AMBER 2007 data in red, to which a fit was made in the H band by fixing θ_{in} to 1 mas and leaving the flux ratio and ring width free. This gives a slightly increased stellar flux contribution of 60% (vs. 55% in the general best-fit model) and a ring width of 4 mas, similar to that in the optical (see Sect. 3.3).

The simple model fits the observations well, as is evidenced by the low χ^2_r values. The best-fit ring is similar in the H and K bands. Particularly in H, but also in K band, a small degeneracy still exists between the ring's inner diameter and

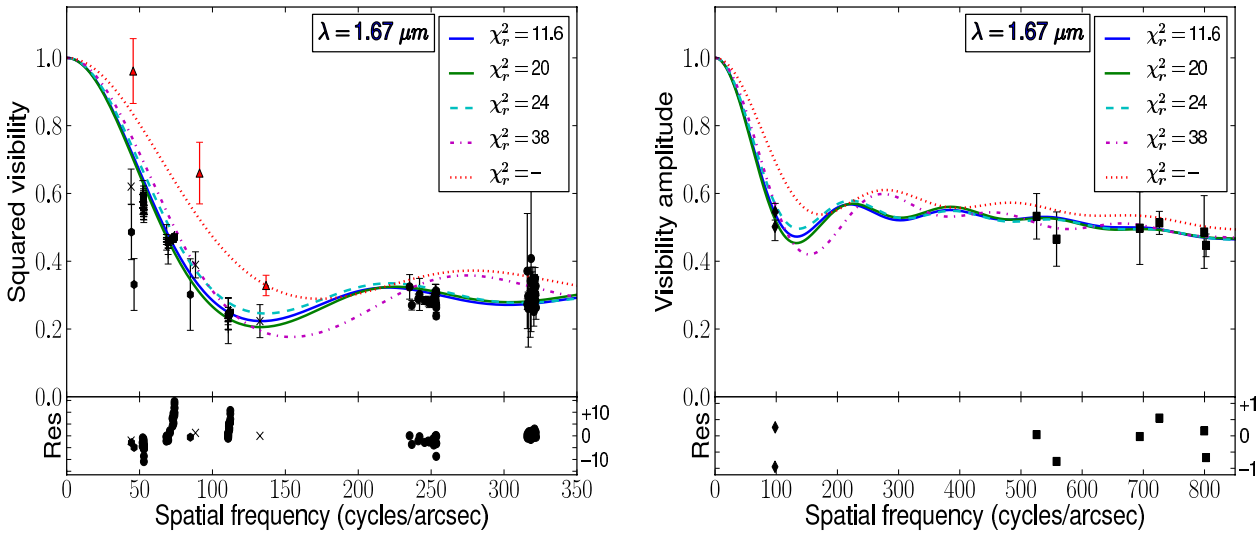

Fig. 3. *Left*: the AMBER (crosses: 2008; pentagons: 2012), PTI (circles) and IOTA (plusses) *H* band squared visibilities. *Right*: the CHARA Array CLASSIC (diamonds) and CLIMB (squares) *H* band visibility amplitudes. The red triangles are the 2007 AMBER data, which are treated separately. In both plots the same five geometric star+ring models are depicted. The full blue and green, dashed cyan, and dot-dashed magenta lines are models with inner diameters and widths equal to 3.0 and 4.6, 4.1 and 4.0, 1.0 and 5.5, and 5.0 and 2.5 mas, respectively. The dotted red line is the best-fit model to the 2007 AMBER data (see text). The legend denotes the χ^2_r value of the corresponding model, except for the red one, which formally has too few data points.

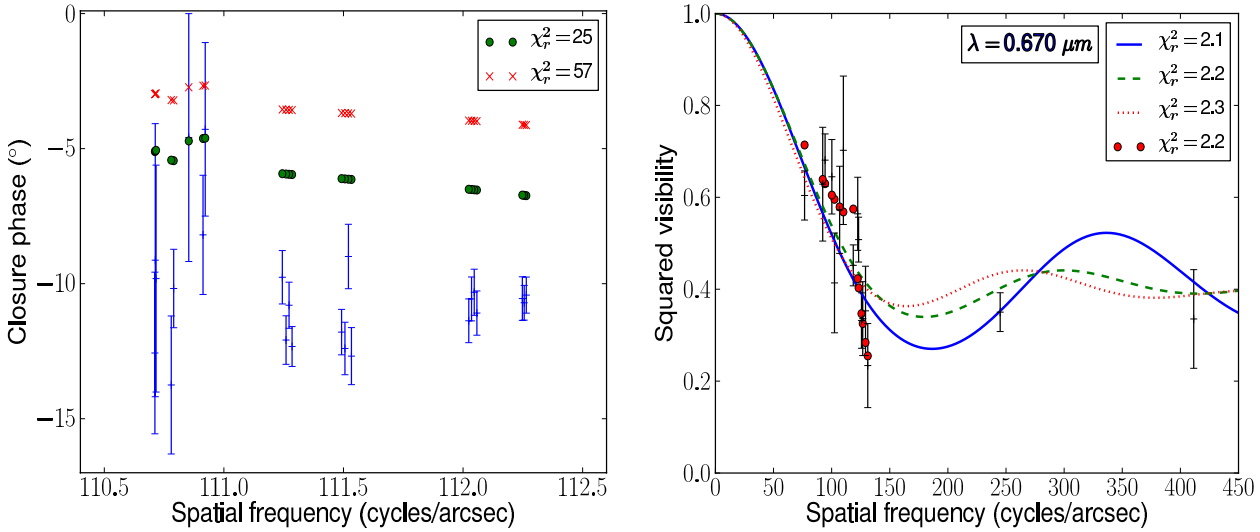

Fig. 5. *Left panel*: the 2003 IOTA closure phases on which the astrometric fit of Sect. 3.4 was based, together with two models, as a function of the maximal spatial frequency in the baseline triangle. The green circles are for a model including only the post-AGB star offset to a position $(x, y) = (-0.4, -0.4)$ mas. The red crosses illustrate the effect of adding the secondary at a position (+0.4, +0.4) mas and contributing 10% of the total flux. *Right panel*: squared visibilities at 673 nm with some models overplotted. The full blue, dashed green, and dotted red lines correspond to star+ring models with ring diameters and widths of (5.5, 1.0), (3.0, 3.0), and (1.0, 4.5), respectively. The red filled circles correspond to the best binary model deduced in Sect. 3.2 and online Fig. 7. The other wavelengths are shown online in Fig. 6. The legend lists the χ^2_r value, which is the same for all four models.

its width, with a slight preference for smaller diameters in combination with larger widths. This means there is flux coming from radii close to the binary orbit, which is in contrast to our original assumption that the emission is coming from dust in a well-localized inner rim. A wide uniform ring works well but is not perfect.

3.2. The central binary in the optical?

As shown in Fig. 5, our measured optical continuum visibilities are lower than expected for a uniform disk (UD) of $\theta_\star$ = 0.45 mas and do not have the spatial frequency dependence of such a simple geometry. It is unlikely that we resolve the binary as the companion is probably still on the main sequence and hence too faint. However, accretion disks, already inferred from spectral monitoring by several authors for similar objects (see, e.g., Witt et al. 2009; Gorlova et al. 2012), are typically hot and can contribute significantly at optical wavelengths, yielding a binary-like signature in the observations. Because the VEGA and NPOI data were obtained at different orbital phases of the binary system, we analyzed the most extensive snapshot, i.e., the NPOI data, first. Already from this analysis, the binary model can be ruled out, as detailed below.

Since the flux ratio can be wavelength dependent, we selected a subset of three wavelengths that cover the full spectral range, i.e., at 562, 673, and 859 nm. Given the lowest squared

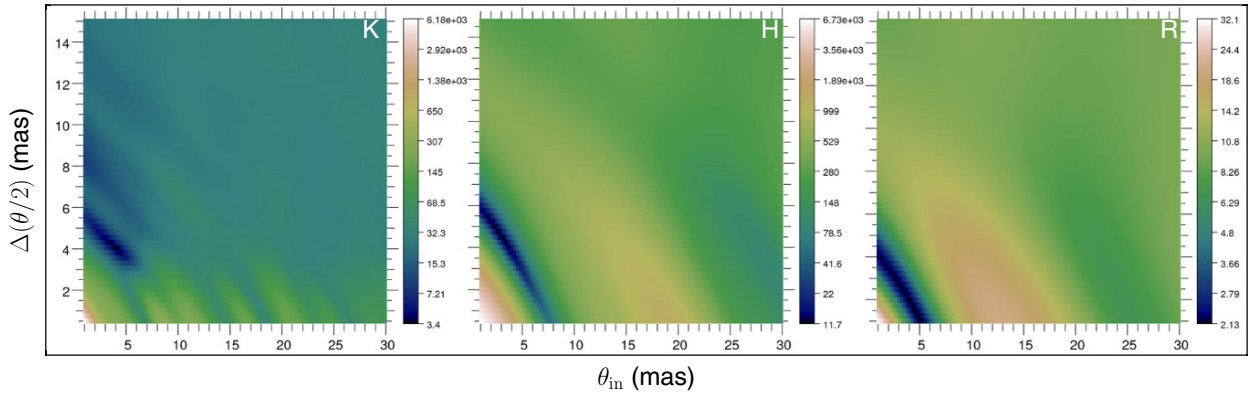

Fig. 8. χ^2_r maps of the ring's geometric parameters for the star+ring model that was fitted to the three different visibility data sets. *From left to right*: *K*, *H* and *R*-band.

visibility of ∼0.2 (Fig. 5), the flux ratio $F_\star/F_{\rm sec}$ should be well within the range {0.2, 5.0}. Starting from equal fluxes and assuming diameters of 0.45 mas for the post-AGB star and 0.5 mas for the accretion disk, we search for the best relative position of both components. Then, the flux ratios and position are iteratively adjusted to find the global minimum. The data do not constrain the flux ratios well, but the exact values do not influence the minimal separation needed to fit the data. Thanks to the good baseline position angle coverage, the positional minimum is rather well defined, except for the 180° ambiguity that can only be resolved with closure phases. The minimal separation is 2 mas (for flux ratios of 5.0, 2.2, and 1.4 at 562, 673, and 859 nm, respectively), and this value does not depend on the exact post-AGB and accretion disk diameters. The squared visibilities of the best-fit binary model are displayed in Figs. 5 and 6, and the χ^2_r map of the secondary's relative position is shown in Fig. 7.

At a distance of 1.5 ± 0.5 kpc, the required angular separation converts into a minimal physical separation of $\rho = 2$ AU at the NPOI epoch. The smallest semi-major axis that can accomodate such a projected separation is for an orbit in which the time of the NPOI measurement would correspond to apastron passage and with $\omega = 0°$. In that limiting case, also assuming the maximal eccentricity of 0.25 (see Table 1), $a = \rho/(1+e) = 1.6$ AU. For 89 Her's period of 288 days, this implies a minimal total system mass of 6.6 $M_\odot$. If the primary is a post-AGB star of ∼0.6 $M_\odot$, the inclination is 3.2°, as derived from the spectroscopic mass function.

However, such a high total mass cannot be reconciled with a post-AGB status for the primary because it would require an extremely efficient mass transfer as well as an original primary mass that is incompatible with the system's high Galactic latitude and the absence of a detected ejection velocity. In addition, there is no signature of the companion's velocity in the optical spectra (Waters et al. 1993; Climenhaga et al. 1987), which is incompatible with the required (from the flux ratio) high luminosity for this putative high-mass companion or its accretion disk. At the minimal distance of 1 kpc, the secondary's luminosity would need to be ∼2100 $L_\odot$ (see Sect. 4). For a 6 $M_\odot$ main sequence star of radius 3 $R_\odot$, this implies an accretion luminosity of ∼1350 $L_\odot$ and hence an accretion rate of $LR/GM = 2\times10^{-5}$ $M_\odot$ yr^{-1}. This rate would be too high to be compatible with the mass loss rate derived from the P Cygni type Hα profile of $\sim10^{-8}$ $M_\odot$ yr^{-1}.

Furthermore, although the inclination of Bujarrabal et al. (2007) is probably not precise to a few degrees, a value of 3° is hard to reconcile with the asymmetry observed in their CO maps. Finally, the near-IR visibilities do not allow for the presence of a low-contrast second stellar-like component (see Sect. 3.4), and no star (or accretion disk at a realistic temperature) is blue enough to be optically bright while being indetectable in the near-IR. We thus conclude that the spatial scale and flux ratio of the central binary do not agree with what is needed to fit our optical interferometry data.

3.3. A ring in the optical

The small inner diameter of the best-fit near-IR ring and the similar scale found with the binary model motivated us to try a ring model to explain our optical data as well. The geometric star+ring model of Sect. 3.1 was fit to all the VEGA and NPOI data. Ring diameters and widths up to 50 mas were tried to allow for a strong scattered light contribution from the outer disk.

The longer baseline VEGA observations are essential to resolve some of the degeneracies between the model parameters, especially to fix the flux ratio more precisely. The fitting strategy was the same as in Sect. 3.1. We adopted a single flux ratio at all wavelengths (see Sect. 4.2). This resulted in a good χ^2_r, while a wavelength-dependent flux ratio does not improve the fit.

Three model visibility curves and the χ^2_r map of the ring diameter versus its width are depicted in Figs. 5 and 8, respectively. A uniform ring fits the optical observations very well. The size of the emitting area is rather small with an outer radius of only 3.5 to 5.5 mas. This agrees well with the fit to the AMBER 2007 data. The inner diameter is not constrained. By changing the flux ratio slightly, the same χ^2_r can be obtained both for an infinitely thin ring at the outer edge (a circle) and for a ring starting at the binary orbit (a disk), and part of the emission may even originate from within it. Independent of the inner diameter, the outer radius of the ring is smaller than in the near-IR.

3.4. Improving the near-IR fit

A circumcompanion accretion disk is not causing the low optical visibilities but could still affect our near-IR data, providing it has a low luminosity and temperature. Although we have good χ^2_r values, the best-fit is still not perfect and results in a rather small inner diameter. A closer look at the near-IR data offers a few arguments against a signature of the secondary in it.

A strong constraint on the secondary's near-IR flux contribution comes from the lack of visibility variations over the orbital cycle on the two PTI baselines. As the binary moves in its orbit, the projected separation onto the fixed baseline changes, thereby

modulating the visibility. The visibility scatter then gives a lower limit on the contrast of the binary. The strongest constraint is derived in the H band because the circumbinary disk dominates the K band. With a continuous phase coverage over a third of the orbital cycle in 2001, we estimate a contrast >5 in the H band.

The strongest contribution to the residuals of the best-fit star+ring model comes from the shortest and longest AMBER baseline in K and from the two shortest IOTA baselines in the H band. A simple way to improve the general fit would be to add a small (~5%) flux component that is fully resolved already at our shortest spatial frequencies. This relaxes the visibility slope in the first lobe and fits with the interpretation of the AMBER 2007 data as being erroneous even in the K band. We note that a proper radiative transfer model, which takes scattering fully into account, typically has such a feature (Pinte et al. 2008). This is because material at radii beyond the inner rim scatters part of the inner rim thermal emission into the line of sight. We note that although part of this flux might fall outside the coherent FOV ($=\lambda^2/(B\Delta\lambda) \sim 20$ mas) at the longest CLIMB baselines, this does not influence any of our results as the dust disk is already fully resolved at these baselines. Our estimation of the flux ratio is thus robust.

Second, we checked the compatibility of the closure phases with the expected post-AGB offset from the phase reference provided by the ring. No constraints could be derived from the AMBER and CLIMB closures due to their large errors, so we present our analysis of the more numerous and precise IOTA data. The expected range of displacements from the center of mass is 0.2–0.5 mas, depending on the distance, spectroscopic orbit, and inclination. Figure 9 (available online) shows the χ^2_r map of the IOTA closure phases as a function of the post-AGB star's position with respect to the best-fit H band ring. Even at the maximal allowed offset, there is a significant difference between the measurements and the model ($\chi^2_r = 12.6$). The measurements are depicted in the left panel of Fig. 5, along with two models. The green circles correspond to a model in which the post-AGB star is positioned at (–0.4, –0.4) mas, which is more realistic than the boundary values preferred by the fit. For the red crosses, the secondary is added at the opposite position as well and contributes 10% of the total flux (corresponding to a flux ratio of ~5). The red model shows that if the secondary is present at the limiting flux contribution determined above, even at a modest separation, the discrepancy between the model and measured closure phases becomes significantly worse.

There are several possibilities to explain the remaining discrepancy. First, the expected displacement could be underestimated, which could imply an overestimated distance. Second, at the given spatial frequencies, the measured closure phases will be strongly influenced by the exact geometry of the circumbinary disk and any deviation from point symmetry in it. Here we approximate the disk with a uniform ring, whose size and width influence the closure phases directly through the cross-terms in the triple product. Given the small inclination, the skewness of the disk is insufficient to induce a strong closure phase signal if it is inherently point-symmetric. An intrinsic asymmetric illumination of the disk might be required to explain the measured closure phases. This would not be hard to imagine, given the close proximity of the best-fit ring to the central object. To properly take these effects into account at the precision level of the IOTA measurements, a detailed radiative transfer model is needed, so we did not try to improve the χ^2_r within the current modeling framework.

3.5. Summarizing remarks

We summarize our interferometric analysis as follows:

1. Our H, K, and optical visibilities, which were collected with different instruments and span a decade in time, are fully consistent with a simple geometric star+ring model.
2. The central post-AGB source only contributes 28 ± 5%, 56 ± 5%, and 65 ± 7% of the total received flux at 2.2, 1.65, and 0.67 μm respectively.
3. Our near-IR data exclude a geometrically thin ring. Part of the emission might stem from close to the central binary.
4. The optical ring can be either geometrically thin or extended, but its outer diameter is smaller than the near-IR one.
5. A low-contrast binary model can fit equally well the optical visibilities but results in an unrealistic binary configuration.
6. Our largest spatial frequencies in H and K, the time series of PTI H visibilities, and the IOTA closure phases rule out the presence of a companion with a contrast ≤5.
7. It is unclear whether our closure phase discrepancy is caused by an inconsistency in the standard orbital parameters, the radial intensity distribution of our uniform ring model, or an azimuthally asymmetric illumination of the inner disk rim.
8. The 2007 AMBER data deviate from all the rest, especially in H and at the shortest baselines. The latter makes an astrophysical interpretation problematic.

4. The SED

4.1. The stellar SED

In our search for the origin of the resolved optical flux, we first re-evaluated the stellar parameters. "Stellar fluxes" are obtained by combining the interferometric flux ratio (Table 5) with the total photometric fluxes. Four photometric bands (V, R, H, and K) were used to refit the SED. This is insufficient to independently constrain all model parameters, i.e., the effective temperature $T_{\rm eff}$, surface gravity $\log g$, metallicity z, interstellar reddening $E(B-V)$, and angular diameter $\theta_\star$. So we restricted some parameters by taking spectroscopic constraints into account, as listed in Table 1. We fix the metallicity to the subsolar value of [Fe/H] = −0.5 and bound $\log g$ to {0.3, 0.8} dex, $T_{\rm eff}$ to {6000, 7000} K, and $E(B-V) < 0.25$ mag.

Since the optical interferometric data correspond to the JOHNSON R band, while the absolute magnitude is better determined in V, we chose to include both. We thus make two assumptions: 1) the stellar flux fraction is the same over the 450 to 850 nm wavelength range; and 2) the archival JOHNSON $V-R$ color of 0.32 mag is not variable. Deviations from these assumptions are expected to be small because a single flux fraction fits the 550–850 nm range well and because the flux-variability is dominated by low-amplitude pulsations that do not affect the $V-R$ color too much. The error is dominated by the absolute uncertainty on the interferometric flux ratios, so our final confidence intervals should be robust. The fitted fluxes are listed in Table 5.

We fit the SED with the Kurucz (1993) model atmospheres. We use the grid-based method of Degroote et al. (2011), which allows us to identify correlations between parameters and to take them into account in determining parameter uncertainties. It uses an χ^2 statistic with five degrees of freedom to determine the goodness of fit and confidence intervals (CI) for the five parameters. In practice, a model SED is corrected for interstellar reddening with the reddening law of Fitzpatrick (2004), then integrated

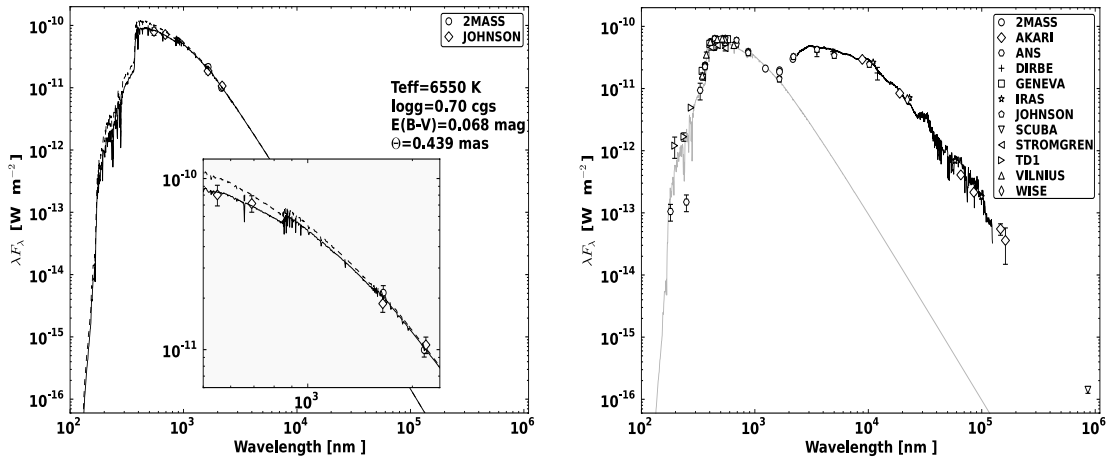

Fig. 11. *Left*: the observed (i.e., reddened, in full) and original (i.e., dereddened, in dashed) stellar SED model plotted over the stellar fluxes. The inset shows a zoom-in on the actual measurements. *Right*: the circumstellar SED (not corrected for reddening), obtained after subtracting the measured total fluxes with the reddened stellar Kurucz model, overplotted with the same reddened Kurucz model (in gray) but with the angular diameter arbitrarily scaled to these circumstellar fluxes. Both panels have the same scales on the x and y axes to illustrate the large amount of circumstellar flux.

over the required photometric passbands, and finally scaled to the measurements by optimizing the angular diameter.

As expected, $T_{\rm eff}$ and $E(B-V)$ are correlated since reddening and effective temperature similarly affect the $V-K$ color. In the literature, different values for both parameters are quoted: based on photometry Luck et al. (1990) adopt $E(B-V) = 0.1$ and find $T_{\rm eff} = 6400$ K, while Waters et al. (1993) find the best fit for $E(B-V) = 0.0$ and $T_{\rm eff} = 6500$ K. Kipper (2011) suggests an $E(B-V) > 0.1$ based on the equivalent width of the interstellar component of the Na I line. Spectroscopic effective temperatures are consistently in the range 6500–6600 K (Luck et al. 1990; Kipper 2011), except for the value of 7177 K found by Takeda et al. (2007). The latter study also found a larger gravity ($\log g = 1.66$) and turbulent velocity ($v_{\rm t} = 8$ km s^{-1}). Finally, the Galactic extinction maps of Arenou et al. (1992), Schlegel et al. (1998), and Drimmel & Spergel (2001) all give $E(B-V) \sim 0.1$ for a distance larger than 1 kpc in the direction of 89 Herculis. We adopt the spectroscopic temperature of 6550 K and $E(B-V) = 0.07 \pm 0.04$, both fully in agreement with our new SED. The derived CI are shown online in Fig. 10.

The $T_{\rm eff}$ and $\theta_\star$, are not correlated strongly: the near-IR fluxes mainly delimit $\theta_\star$ since they are in the Rayleigh-Jeans regime. Our final angular diameter, at $T_{\rm eff} = 6550$ K, is $\theta_\star = 0.435 \pm 0.008$ mas, which is perfectly within the range determined in Sect. 3.1 based on the H band interferometric data. The final stellar SED models are shown in the left panel of Fig. 11.

We made a stellar luminosity histogram by sampling the model parameter space according to our derived probabilities. Model bolometric fluxes are converted into luminosities by assuming a distance of 1.5 kpc. Following the measured parallax, this is the distance with the highest probability. Due to Lutz-Kelker bias and the rather large error on the parallax, it is likely an underestimate of the true distance and hence of the derived luminosity. In general, our results are unaffected by this large uncertainty since the same distance is consistently used to convert the interferometric angular quantities into physical scales. By imposing the spectroscopic constraint on $T_{\rm eff}$, we adopt a final luminosity of 8350 $L_\odot$, the median value of the subset of the histogram shown in Fig. 12. As a comparison, we also show the histograms that would be obtained without our flux ratio correction (selecting only photometry up to J band). The median luminosity is then 13 400 $L_\odot$.

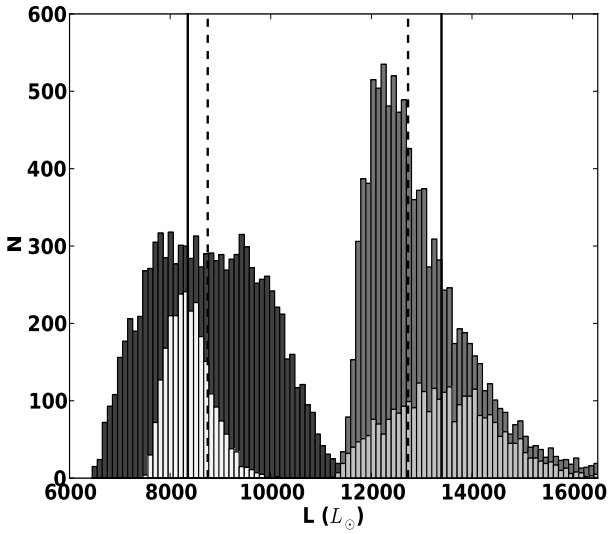

Fig. 12. Luminosity histogram of the stellar SED fit. The *left and right* histograms show the results of the fit to the flux ratio corrected and total photometry, respectively. The full histogram (10 000 points) is shown in dark gray, while the light gray subsamples were obtained thanks to the spectroscopic temperature constraint. The full and dashed lines are the median values of the light and dark histograms, respectively, and have values of 8350 and 8750 $L_\odot$ for our revised stellar photometry. The histograms were made assuming a distance of 1.5 kpc.

4.2. The circumstellar SED

The "circumstellar SED", obtained by subtracting the stellar SED from the total fluxes, is shown in the right panel of Fig. 11, together with the stellar (but rescaled) Kurucz model. Figure 13 contains the calibrated Hermes spectral shapes. Overplotted are three similarly convolved and scaled stellar Kurucz models with $E(B-V) = 0.02$, 0.07, and 0.12 for the upper dashed, full, and lower dashed line, respectively. The observations follow the best-fit stellar model with $E(B-V) = 0.07$ in both figures, although a careful inspection of the Hermes spectral slopes shows that the measurements are slightly bluer in the 500–700 nm range. This could be due to (the more abundant) small emission lines or to a residual in the calibration. The Hermes spectrum is

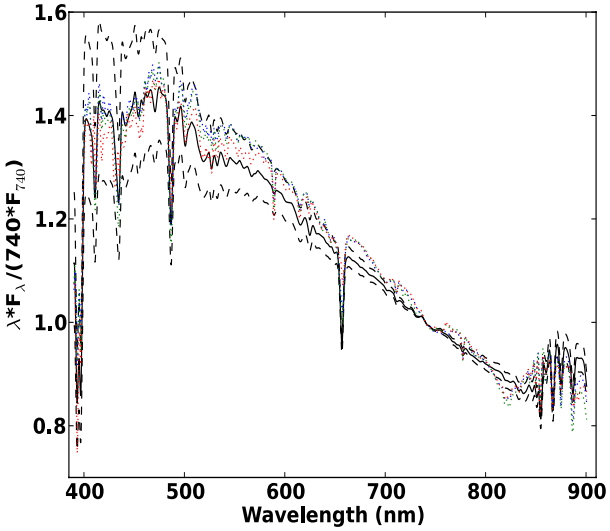

Fig. 13. Hermes spectral shapes (dotted lines, colors denote the observation epoch) compared to spectral shapes from different atmosphere models convolved to the same resolution. The full black line is the model shown in Fig. 11. The dashed lines have the same parameters, except for the reddening, which is $E(B-V) = 0.12$ and 0.02 for the lower and upper line, respectively.

the sum of the stellar and circumstellar contribution. So the absence of a color difference between the measured spectral shape and that of the star alone independently confirms that the process responsible for the circumstellar flux is essentially gray over the whole optical wavelength range.

A basic quantity, often used as a proxy for the scaleheight of a passive dusty disk, is the ratio of the infrared excess over the stellar bolometric flux $F_{\rm IR}/F_\star$. Dominik et al. (2003) estimate the disk's half-opening angle α by approximating the disk as an optically thick cylinder that redistributes all received flux isotropically. The height of this cylinder determines which fraction of the stellar luminosity is intercepted. However, their derivation is only valid for small opening angles. Following their line of reasoning, one can more generally write

$$F_{\rm IR} = \frac{L_\star}{4\pi R^2} 8\pi R^2 \sin^2(\alpha/2) \frac{\pi D^2}{4\pi d^2} \quad (1)$$

and

$$F_\star = \frac{L_\star}{4\pi d^2} \pi D^2, \quad (2)$$

with $L_\star$ the stellar luminosity, d the distance to the observer, and D the diameter of the observer's collecting area. Here, the fraction of the total solid angle subtended by the disk, as viewed from the star, is $8\pi R^2 \sin^2(\alpha/2)$, computed by integrating a sphere azimuthally and between polar angles α and $-\alpha$. This leads to the relation

$$\frac{F_{\rm IR}}{F_\star} = 2\sin^2(\alpha/2) \quad (3)$$

and a half-opening angle of $\alpha = 67.5°$ (see Fig. 14), obtained by integrating our revised stellar SED and the IR part of our circumstellar SED ($F_{\rm IR}/F_\star = 0.62$). If the large fraction of circumstellar scattered light is included as well, then we find a ratio of reprocessed over stellar flux of $F_{\rm RP}/F_\star = 1.29$. In the isotropic approximation, $F_{\rm RP}/F_\star$ cannot become larger than one. Clearly, a significantly nonisotropic process must be at work in the 89 Her system.

Finally, we emphasize that our finding of an essentially gray circumstellar flux is not fully independent from our previous assumptions. A wavelength-dependent flux ratio between 0.56 and 0.85 μm is possible since our observations are not very sensitive to this. Although our CI were determined conservatively as they are dominated by the error on the optical flux ratio, a significant wavelength dependence could result in an underestimated $E(B-V)$ upper limit. The angular diameter is not affected since our near-IR flux ratios are more robust. Our $F_\star$ follows directly from $\theta_\star$ and the spectroscopic $T_{\rm eff}$ and is independent of the reddening, while $F_{\rm RP}$ depends on it twice. First, the circumstellar fluxes in the blue part of the SED are an extrapolation: they are obtained by subtracting the *reddening-dependent* stellar Kurucz model from the measured (and still reddened) fluxes. Second, these reddened circumstellar fluxes need to be dereddened to obtain $F_{\rm RP}$. So our derived $F_{\rm RP}/F_\star$ can still be underestimated, and the circumstellar flux would then be blue instead of gray.

5. Discussion

In this study we present the first multiwavelength long-baseline interferometric data of a post-AGB binary with circumbinary disk that covers wavelengths from 0.55 to 2.5 μm. Our most intriguing result is the discovery of a strong resolved optical flux component. We considered two geometric models to explain our observations: a binary and a star+ring, which both technically fit our optical data equally well based on their χ^2_r. Nevertheless, we argue that the binary model is hard to understand in terms of our near-IR data as well as from a physical point of view. A star+ring model offers a more natural explanation for all our optical visibilities and is compatible in size with our near-IR findings. The optical ring can range from thin with a diameter of 5.5 ± 1.0 mas (a circle) to extended with an outer diameter of 10 ± 2 mas (a UD). Our analysis of the SED and the Hermes spectral slopes showed that the spectrum of the extended emission is very similar to that of the post-AGB star, which strongly suggests a scattering process as its origin.

In the following we discuss three ways to explain our observations (see Fig. 14). Given the similarities between post-AGB and protoplanetary disks, we relate our results to both of them.

5.1. Simply the circumbinary disk

In the simplest case, all optical flux is light scattered off the inner rim of the dust disk. The question is whether a passive disk can reach the necessary scaleheight and redirect the required fraction of the stellar luminosity into our direction. Although estimated from very simple considerations, the large α of 67.5° shows that even to just account for the IR excess the disk already needs a large scaleheight. This could be favorable to account for the optical scattered light. Asymmetric scattering is preferentially forward directed (see, e.g., Mulders et al. 2013), so with the small inclination of ~12°, our viewing angle onto the system is very unfavorable unless there is material high enough above the orbital plane. Quantitatively, this also depends on the properties of the dust, such as composition and grain size. However, it remains to be seen whether the optical and near-IR fluxes and visibilities can be made compatible in this geometry. A circumbinary disk with a very large scaleheight might result in a too thin, circle-like, near-IR emission geometry. The optical visibilities are, however, compatible with the near side of the disk being brighter in scattered light, given the good fit of both a binary

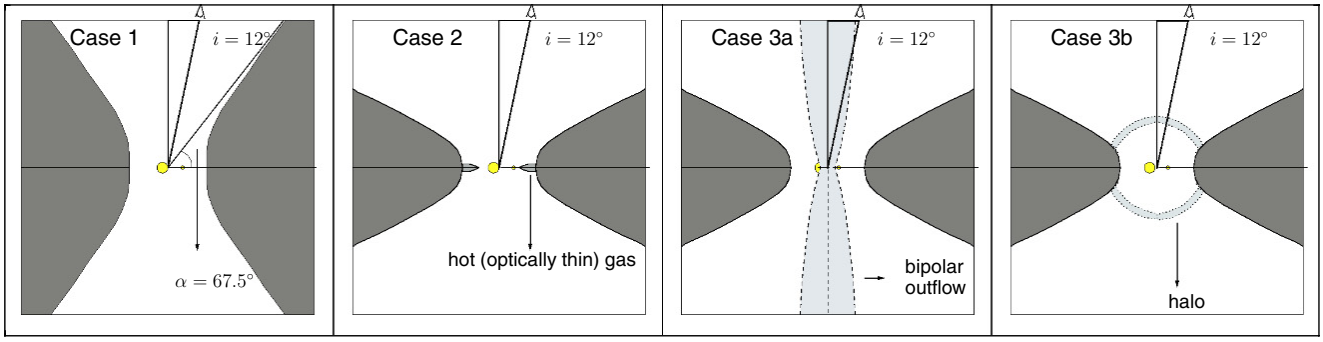

Fig. 14. Pictographic representations of the different geometries that are discussed in Sect. 5.

and a star+ring model to the NPOI observations. Detailed radiative transfer modeling is required to tell whether this geometry is realistic. Here we restrict ourselves to a qualitative discussion.

Protoplanetary disks have been well studied in scattered-light images, especially with the HST (see, e.g., Grady et al. 2013; Cox et al. 2013; Mulders et al. 2013, and references therein), but also with Subaru 8.2 m near-IR coronagraphic imaging (Fukagawa et al. 2004, 2006) and sparse aperture masking experiments or adaptive optics imaging on the VLT (Cieza et al. 2013) or Keck (McCabe et al. 2011; Tuthill et al. 2001). These and other studies find integrated scattered light flux ratios of up to a few percent, while we find that 35–40% of the total optical flux is resolved. All the above methods have a limiting resolution of ~30–50 mas, which corresponds to 5–10 AU for the nearest star-forming regions at 200 pc. For all but the brightest Herbig Be sources, these scales probe the bulk of the disk and not the inner rim. Near-IR interferometers do have the required resolution, and many inner rim regions have been resolved in this way (see further). However, at these wavelengths and with their typically sparse uv coverage, it is impossible to make a distinction between thermal and scattered light, contrary to the current study. To our knowledge, the only optical study of a protoplanetary disk and at a similar angular, but ten times higher spatial, resolution are the results on AB Aur with CHARA/VEGA (Rousselet-Perraut et al. 2010). They resolved the Hα line-forming region at sub-AU scales but found the continuum to be unresolved. Bonneau et al. (2011) did find a 15%, fully resolved, optical continuum flux from a circumbinary dust reservoir in the interacting binary system ν Sgr, but it had rather large error bars.

No published radiative transfer disk model, at viewing angles close to pole-on, has yet predicted such a large optical scattered flux as is found here. This implies that if we probe scattered light off the inner rim, the models are either lacking an important ingredient or post-AGB disks are different from protoplanetary ones or even 89 Her is special in some way. In any case, evolved star disks are likely to be more puffed up than protoplanetary ones, given their high luminosities and small central masses.

5.2. The circumbinary disk + an inner gas disk

Our results show a preference for an extended emission region, starting close to the central object. Since dust only survives beyond the sublimation radius, some of this flux may be gaseous emission from within the inner rim. This is not unlikely given the detection of CO emission at 2.3 μm, needing temperatures >2000 K.

Such gaseous emission was often suggested in the literature as the missing component to explain near-IR interferometric data of protoplanetary disks. Monnier & Millan-Gabet (2002) found that certain high-luminosity sources are seriously undersized with respect to their size-luminosity relation. This was later confirmed (Monnier et al. 2005; Eisner et al. 2004) and attributed to the presence of a (geometrically thin, but optically thick?) gaseous disk within the dust sublimation radius. More evidence was claimed in the studies of Akeson et al. (2005) for some T Tauri stars and in the studies of Kraus et al. (2008) and Tannirkulam et al. (2008) for some Herbig Ae/Be sources. Only the latter study had a sufficient spatial resolution to resolve the K band continuum emission from within the expected inner rim. Its authors attempted to empirically derive the sources of opacity responsible for the emission from the spectral shape of the flux-deficit between 1.25 and 10 μm. A slight preference for free-free and bound-free opacity of H^- (5000 K) or neutral hydrogen (8000 K) was found over a mixture dominated by molecular opacity (2000–2500 K), which was due to the lack of strong molecular features between 4 and 10 μm. The H^- and neutral hydrogen models overshoot their observations at wavelengths $\leq$2 μm and produce a significant optical flux. However, they did not investigate whether such extreme conditions are physically realistic.

A more extensive data set on HD 163296, one of the targets in Tannirkulam et al. (2008), was presented by Benisty et al. (2010) and compared to simple gaseous disk models in a bit more detail. The optically thick models of Muzerolle et al. (2004) were similarly rejected because of the absence of strong molecular emission features in the SED. Additionally, they presented SEDs of non-local thermodynamic equilibrium (non-LTE) gaseous components with varying densities and temperatures and showed its spectral dependence to be incompatible with the observations. It might be tempting to interpret our resolved optical flux in terms of these hot gas models, but the latter argument also holds for 89 Her. While H^- is the foremost source of continuum opacity below 8000 K, bound-free processes dominate above it. In both cases the spectral dependence is incompatible with our smooth circumstellar SED. The H^- opacity reaches a maximum value at 850 nm and drops steeply shortwards.

Moreover, the source function needs a temperature >4500 K (assuming optically thick radiation) over the full emitting surface area to reproduce our visibilities and fluxes. Close to the illuminating source, the combination of such a temperature with a reasonable density (hence optical depth) *might* be attainable. But due to flux dilution, the temperature drops quickly with radius as a power law with exponents of 1/2 and 3/4 for a flaring or flat reprocessing disk, respectively (Kenyon & Hartmann 1987).

Given the large size of the post-AGB star and our observations that do not support a bright companion, accretion energy cannot contribute significantly. Since the density also drops with radius, the disk becomes too optically thin at large radii very quickly. By decoupling the gas from the dust temperature, Woitke et al. (2009) found in their detailed thermochemical protoplanetary disk models a hot surface layer that bends around the inner rim with temperatures in excess of 4000 K. However, the density in this small region is too low to produce a significant continuum optical depth and flux. On the other hand, Muzerolle et al. (2004) found typical temperatures of only ~1100 K (assuming LTE opacities), even close to the central star. All these models are very crude and as Benisty et al. (2010) remarked, more realistic models that treat the transition from optically thin to optically thick gas layers in a dust-free environment are needed to definitely rule out inner gas disks as a dominant effect.

Alternatively, Benisty et al. (2010) proposed an inner dusty disk consisting of highly refractory grains that manage to survive the low-pressure, high-temperature environment within the inner rim of the "silicate-disk". This model reproduced their near-IR interferometric data perfectly but required high temperatures of ~2200 K at the inner radius. Using a more sophisticated treatment of dust sublimation and condensation physics within a Monte Carlo radiative transfer code, Kama et al. (2009) also found solutions with a large optically thin region, covering up to 70% of the surface inside the inner rim. This geometry offers advantages as it allows for the existence of a large surface within the actual rim with possibly a distinct grain population. However, from a scattering perspective, the small geometric thickness of this region makes it energetically an unlikely option to account for our optical observations.

5.3. The circumbinary disk + a (bipolar) outflow

The emission morphology might be more complex. The rather large errors on the NPOI visibilities prevent a firm conclusion on any position angle dependence of the visibility, but the good fit of the binary model shows that it cannot be excluded either. A bipolar outflow seen pole-on, originating as a stellar wind or jet, might naturally give rise to the presence of small-scale structure, including arc or knot-like features. There are several arguments in favor of this model. First, there is the large-scale hour-glass-like nebula discovered by Bujarrabal et al. (2007), which must have an origin in the central object. Second, bipolar outflows are commonly inferred to explain high-resolution spectroscopic time series of many classes of evolved binaries, in particular post-AGB ones like the Red Rectangle (Witt et al. 2009; Thomas et al. 2011, 2013) or BD+46°442 (Gorlova et al. 2012). The weak, neutral or low-excitation-level emission lines of metals (e.g. Fe I near 805 nm) were already interpreted by Waters et al. (1993) in terms of a collisionally excited interaction between a modest stellar wind and the circumbinary disk. The same lines, which are variable in strength but not in velocity, are seen in emission in QY Sge (Kameswara Rao et al. 2002) and BD+46°442 (Gorlova et al. 2012), but with a different width that the latter authors suggest to be an inclination effect. Also, the weak and variable Hα P Cygni profile is a clear indication for a small mass loss rate of $\sim 10^{-8}$ $M_\odot$ yr^{-1} (Sargent & Osmer 1969). The main question in this outflow scheme is why the scattered light is so well confined to the size of the disk inner rim (compare the panels in Fig. 8).

Jets or bipolar outflows are often detected around YSOs for a wide range of central masses, and their presence is strongly linked to accretion phenomena (Königl 1999). These jets are detected over the full electromagnetic spectrum, most notably through maser, free-free, and synchrotron emission at radio wavelengths, IR molecular tracers, and in shock-excited near-IR/optical/UV spectral lines (Bally 2007). For highly obscured objects, significant bipolar reflection nebulae are seen and interpreted as scattering by dusty material within or on the walls of the outflow cavities produced by the jet (Padgett et al. 1999).

A similar explanation (but with a different origin for the dust) has been given for the HST images of bipolar planetary (PNe) and proto-planetary nebulae (PPNe) in scattered light (Kwok et al. 1998, 2000; Ueta et al. 2000; Bujarrabal et al. 2002; Cohen et al. 2004; Siódmiak et al. 2008). Post-AGB binaries are classified as "stellar" in these HST surveys, which is corroborated by the small scale of the optical circumstellar flux found here.

Based on optical and UV spectropolarimetry, Joshi et al. (1987) claim the presence of two geometrically distinct dust populations around HR4049, which consist of differently sized particles. Later, Johnson et al. (1999) confirm this result and associate the component with the smallest particles ($\leq$0.05 μm), seen mainly at wavelengths <2000 Å, with a bipolar structure. Joshi et al. (1987) found for 89 Her an even larger degree of polarization than for HR4049, but without the latter's PA dependence.

The main advantage of an outflow is that it allows having material at a high altitude above the disk midplane that can efficiently (forward-)scatter light into our line of sight that would otherwise freely escape. Although contested, optically thin halos are an alternative way to do this and are often inferred to explain (near-IR resolved) data of protoplanetary disks (Chen et al. 2012; Verhoeff et al. 2011; Mulders et al. 2010). Explanations for halo formation range from collisions between planetesimals with highly inclined orbits (Krijt & Dominik 2011) to dust entrainment in upper disk layers, where dust and gas are not thermally coupled (Woitke et al. 2009) and the gas thus has a higher vertical extension (Verhoeff et al. 2011). In any case, "halos" are likely too optically thin if they are dynamically stable. In the model of Verhoeff et al. (2011), the halo contributes at most 10% of the stellar optical flux.

6. Conclusions

Our optical interferometric data show that one should be careful not to overlook a possible scattering component when establishing the energy budget in systems with significant circumstellar material as derived from the IR excess. By separating the direct stellar light from the reprocessed, circumstellar light between 0.5 and 2.2 μm, we reassessed the stellar and circumstellar SED and revised the stellar luminosity of 89 Her from 13 400 to 8350 $L_\odot$, assuming a distance of 1.5 kpc. This lower luminosity corresponds to a decrease in angular (and thus also physical) diameter from the previously assumed ~0.65 to the directly measured 0.435 ± 0.008 mas.

The circumstellar luminosity is then likewise increased, resulting in a ratio of $F_{\rm IR}/F_\star = 0.62$ and $F_{\rm RP}/F_\star = 1.29$. The former leads to a large half-opening angle of the circumbinary disk of 67.5° *if* all the observed IR circumstellar flux is reprocessed light by the disk. The latter, on the other hand, requires a nonisotropic process. In Paper II we will use a radiative transfer code to test whether a passive circumbinary disk can be created that reproduces our observations.

Alternatively, adding geometric components could ease the requirements on the scaleheight of the disk, and we discussed several possibilities. A bipolar outflow is an interesting option from an evolutionary perspective but requires explanation in

terms of projected size. A vertical extension of the disk into a kind of halo is also possible, but might be too optically thin. An inner gas disk is deemed unlikely, but definite exclusion of it requires more realistic models in non-LTE conditions.

Our redefined SEDs show that the circumstellar energy budget is already dominated by scattered light in *H* band. Compared to the *K* band, we find a slight preference for a smaller (projected) emission region in *H* band and a clear preference in the optical, which could be a hint for the presence of material above the orbital plane that mainly contributes through scattering.

An important consequence of our findings is that determining luminosities of post-AGB binaries from SED fitting is even more complex than previously assumed. On top of the difficulties related to inclination, reddening, and distance (still the dominant source of uncertainty), one now also has to take into account a possibly dominant scattered light contribution. Its exact origin decides whether 89 Her is an extreme or average case and what will be the spread in scattered light fractions for other objects. If resolved observations are the only way to detect this extended optical emission, a detailed comparison of post-AGB objects with evolutionary tracks might become problematic because LMC sources cannot be resolved spatially and distances to galactic sources will remain uncertain, at least until the Gaia satellite comes online.

Acknowledgements. M.H. wishes to thank B. Acke and C. Dominik for the useful discussions about this work and P. Degroote for his SED-fitting scripts. The Navy Precision Optical Interferometer is a joint project of the Naval Research Laboratory and the US Naval Observatory, in cooperation with Lowell Observatory, and is funded by the Office of Naval Research and the Oceanographer of the Navy. The authors would like to thank Jim Benson and the NPOI observational support staff, whose efforts made this project possible. The CHARA Array is funded by the National Science Foundation through NSF grant AST-0606958, by Georgia State University through the College of Arts and Sciences, and by the W.M. Keck Foundation. The Palomar Testbed Interferometer was operated by the NASA Exoplanet Science Institute and the PTI collaboration. It was developed by the Jet Propoulsion Laboratory, California Institute of Technology, with funding provided from the National Aeronautics and Space Administration. This work has made use of services produced by the NASA Exoplanet Science Institute at the California Institute of Technology. The IOTA data would not have been possible without contributions from Mark Swain, Ettore Pedretti, Wes Traub, J.-P. Berger, and Rafael Millan-Gabet. We also thank SAO, U. Mass, NSF AST-0138303, NSF AST-0352723, and NASA NNG05G1180G for supporting IOTA development and operations.

References

Akeson, R. L., Walker, C. H., Wood, K., et al. 2005, ApJ, 622, 440
Arenou, F., Grenon, M., & Gomez, A. 1992, A&A, 258, 104
Armstrong, J. T., Mozurkewich, D., Rickard, L. J., et al. 1998, ApJ, 496, 550
Bally, J. 2007, Ap&SS, 311, 15
Banerjee, D. P. K., & Ashok, N. M. 2002, A&A, 395, 161
Benisty, M., Natta, A., Isella, A., et al. 2010, A&A, 511, A74
Berger, J.-P., Haguenauer, P., Kern, P. Y., et al. 2003, in SPIE Conf. Ser., 4838, ed. W. A. Traub, 1099
Boden, A. F., Colavita, M. M., van Belle, G. T., & Shao, M. 1998, in SPIE Conf. Ser., 3350, ed. R. D. Reasenberg, 872
Bonneau, D., Clausse, J.-M., Delfosse, X., et al. 2006, A&A, 456, 789
Bonneau, D., Chesneau, O., Mourard, D., et al. 2011, A&A, 532, A148
Bujarrabal, V., Alcolea, J., Sánchez Contreras, C., & Sahai, R. 2002, A&A, 389, 271
Bujarrabal, V., van Winckel, H., Neri, R., et al. 2007, A&A, 468, L45
Chelli, A., Utrera, O. H., & Duvert, G. 2009, A&A, 502, 705
Chen, L., Kreplin, A., Wang, Y., et al. 2012, A&A, 541, A104
Cieza, L. A., Lacour, S., Schreiber, M. R., et al. 2013, ApJ, 762, L12
Climenhaga, J. L., Smoliński, J., Krempeć-Krygier, J., Krygier, B., & Krawczyk, S. 1987, in Circumstellar Matter, eds. I. Appenzeller, & C. Jordan, IAU Symp., 122, 329
Cohen, M., Van Winckel, H., Bond, H. E., & Gull, T. R. 2004, AJ, 127, 2362
Colavita, M. M. 1999, PASP, 111, 111
Colavita, M. M., Wallace, J. K., Hines, B. E., et al. 1999, ApJ, 510, 505
Cox, A. W., Grady, C. A., Hammel, H. B., et al. 2013, ApJ, 762, 40
Cutri, R. M., et al. 2012, VizieR Online Data Catalog, II/311
de Ruyter, S., van Winckel, H., Maas, T., et al. 2006, A&A, 448, 641
Degroote, P., Acke, B., Samadi, R., et al. 2011, A&A, 536, A82
Deroo, P., van Winckel, H., Min, M., et al. 2006, A&A, 450, 181
Deroo, P., Acke, B., Verhoelst, T., et al. 2007, A&A, 474, L45
Dominik, C., Dullemond, C. P., Cami, J., & van Winckel, H. 2003, A&A, 397, 595
Drimmel, R., & Spergel, D. N. 2001, ApJ, 556, 181
Ducati, J. R. 2002, VizieR Online Data Catalog, II/237
Dullemond, C. P., & Monnier, J. D. 2010, ARA&A, 48, 205
Eisner, J. A., Lane, B. F., Hillenbrand, L. A., Akeson, R. L., & Sargent, A. I. 2004, ApJ, 613, 1049
Fitzpatrick, E. L. 2004, in Astrophysics of Dust, eds. A. N. Witt, G. C. Clayton, & B. T. Draine, ASP Conf. Ser., 309, 33
Frankowski, A., & Jorissen, A. 2007, Balt. Astron., 16, 104
Fukagawa, M., Hayashi, M., Tamura, M., et al. 2004, ApJ, 605, L53
Fukagawa, M., Tamura, M., Itoh, Y., et al. 2006, ApJ, 636, L153
Gielen, C., Bouwman, J., van Winckel, H., et al. 2011, A&A, 533, A99
Gorlova, N., Van Winckel, H., Gielen, C., et al. 2012, A&A, 542, A27
Grady, C. A., Muto, T., Hashimoto, J., et al. 2013, ApJ, 762, 48
Hummel, C. A., Benson, J. A., Hutter, D. J., et al. 2003, AJ, 125, 2630
Johnson, J. J., Anderson, C. M., Bjorkman, K. S., et al. 1999, MNRAS, 306, 531
Joshi, U. C., Deshpande, M. R., Sen, A. K., & Kulshrestha, A. 1987, A&A, 181, 31
Kama, M., Min, M., & Dominik, C. 2009, A&A, 506, 1199
Kameswara Rao, N., Goswami, A., & Lambert, D. L. 2002, MNRAS, 334, 129
Kenyon, S. J., & Hartmann, L. 1987, ApJ, 323, 714
Kipper, T. 2011, Balt. Astron., 20, 65
Königl, A. 1999, New Astron. Rev., 43, 67
Kraus, S., Preibisch, T., & Ohnaka, K. 2008, ApJ, 676, 490
Krijt, S., & Dominik, C. 2011, A&A, 531, A80
Kurucz, R. L. 1993, VizieR Online Data Catalog, VI/39
Kwok, S., Hrivnak, B. J., & Su, K. Y. L. 2000, ApJ, 544, L149
Kwok, S., Su, K. Y. L., & Hrivnak, B. J. 1998, ApJ, 501, L117
Lagadec, E., Verhoelst, T., Mékarnia, D., et al. 2011, MNRAS, 417, 32
Luck, R. E., Bond, H. E., & Lambert, D. L. 1990, ApJ, 357, 188
Mastrodemos, N., & Morris, M. 1998, ApJ, 497, 303
McCabe, C., Duchêne, G., Pinte, C., et al. 2011, ApJ, 727, 90
Mérand, A., Bordé, P., & Coudé du Foresto, V. 2005, A&A, 433, 1155
Mermilliod, J.-C., Mermilliod, M., & Hauck, B. 1997, A&AS, 124, 349
Millan-Gabet, R., Schloerb, F. P., & Traub, W. A. 2001, ApJ, 546, 358
Molster, F. J., Waters, L. B. F. M., Tielens, A. G. G. M., & Barlow, M. J. 2002, A&A, 382, 184
Monnier, J. D., & Millan-Gabet, R. 2002, ApJ, 579, 694
Monnier, J. D., Millan-Gabet, R., Billmeier, R., et al. 2005, ApJ, 624, 832
Monnier, J. D., Berger, J.-P., Millan-Gabet, R., et al. 2006, ApJ, 647, 444
Mourard, D., Clausse, J. M., Marcotto, A., et al. 2009, A&A, 508, 1073
Mulders, G. D., Dominik, C., & Min, M. 2010, A&A, 512, A11
Mulders, G. D., Min, M., Dominik, C., Debes, J. H., & Schneider, G. 2013, A&A, 549, A112
Murakami, H., Baba, H., Barthel, P., et al. 2007, PASJ, 59, 369
Muzerolle, J., D'Alessio, P., Calvet, N., & Hartmann, L. 2004, ApJ, 617, 406
Padgett, D. L., Brandner, W., Stapelfeldt, K. R., et al. 1999, AJ, 117, 1490
Petrov, R. G., Malbet, F., Weigelt, G., et al. 2007, A&A, 464, 1
Pinte, C., Ménard, F., Berger, J. P., Benisty, M., & Malbet, F. 2008, ApJ, 673, L63
Raskin, G., van Winckel, H., Hensberge, H., et al. 2011, A&A, 526, A69
Rousselet-Perraut, K., Benisty, M., Mourard, D., et al. 2010, A&A, 516, L1
Sargent, W. L. W., & Osmer, P. S. 1969, in Mass Loss from Stars, ed. M. Hack, Astrophys. Space Sci. Lib., 13, 57
Schlegel, D. J., Finkbeiner, D. P., & Davis, M. 1998, ApJ, 500, 525
Siódmiak, N., Meixner, M., Ueta, T., et al. 2008, ApJ, 677, 382
Smith, B. J., Price, S. D., & Baker, R. I. 2004, ApJS, 154, 673
Takeda, Y., Taguchi, H., Yoshioka, K., et al. 2007, PASJ, 59, 1127
Tallon-Bosc, I., Tallon, M., Thiébaut, E., et al. 2008, in SPIE Conf. Ser. 7013
Tannirkulam, A., Monnier, J. D., Harries, T. J., et al. 2008, ApJ, 689, 513
Tatulli, E., Millour, F., Chelli, A., et al. 2007, A&A, 464, 29
ten Brummelaar, T. A., McAlister, H. A., Ridgway, S. T., et al. 2005, ApJ, 628, 453
ten Brummelaar, T. A., Sturmann, J., McAlister, H. A., et al. 2012, in SPIE Conf. Ser., 8445
Thomas, J. D., Witt, A. N., Aufdenberg, J. P., et al. 2011, MNRAS, 417, 2860
Thomas, J. D., Witt, A. N., Aufdenberg, J. P., et al. 2013, MNRAS, 585

Thompson, G. I., Nandy, K., Jamar, C., et al. 1978, Catalogue of stellar ultraviolet fluxes. A compilation of absolute stellar fluxes measured by the Sky Survey Telescope (S2/68) aboard the ESRO satellite TD-1
Traub, W. A., Ahearn, A., Carleton, N. P., et al. 2003, in SPIE Conf. Ser. 4838, ed. W. A. Traub, 45
Tuthill, P. G., Monnier, J. D., & Danchi, W. C. 2001, Nature, 409, 1012
Ueta, T., Meixner, M., & Bobrowsky, M. 2000, ApJ, 528, 861
van Aarle, E., van Winckel, H., Lloyd Evans, T., et al. 2011, A&A, 530, A90
van Belle, G. T., van Belle, G., Creech-Eakman, M. J., et al. 2008, ApJS, 176, 276
van Winckel, H. 2003, ARA&A, 41, 391
van Leeuwen, F. 2007, A&A, 474, 653
Van Winckel, H., Hrivnak, B. J., Gorlova, N., Gielen, C., & Lu, W. 2012, A&A, 542, A53
van Winckel, H., Lloyd Evans, T., Briquet, M., et al. 2009, A&A, 505, 1221
Verhoeff, A. P., Min, M., Pantin, E., et al. 2011, A&A, 528, A91
Wallace, L., & Hinkle, K. 1997, ApJS, 111, 445
Waters, L. B. F. M., Waelkens, C., Mayor, M., & Trams, N. R. 1993, A&A, 269, 242
Wesselius, P. R., van Duinen, R. J., de Jonge, A. R. W., et al. 1982, A&AS, 49, 427
Witt, A. N., Vijh, U. P., Hobbs, L. M., et al. 2009, ApJ, 693, 1946
Woitke, P., Kamp, I., & Thi, W.-F. 2009, A&A, 501, 383

Pages 15 to 17 are available in the electronic edition of the journal at http://www.aanda.org

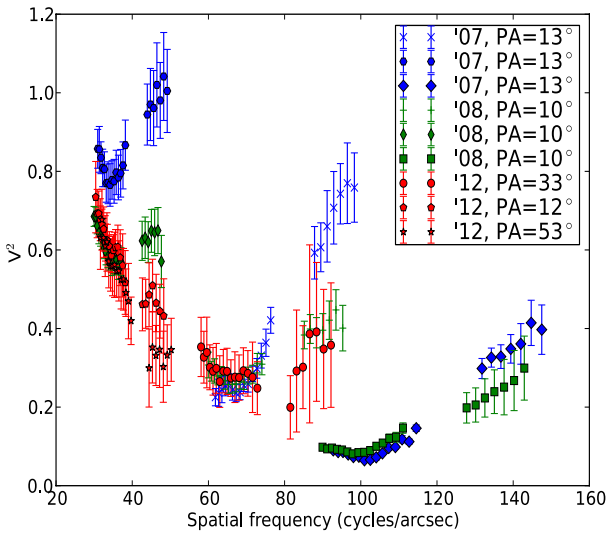

Fig. 2. AMBER (LR-HK) squared visibilities as a function of the spatial frequency. The legend denotes the epoch and the position angle (PA) of the baseline of the observation. All 2007 and 2008 data have a similar PA because the same co-linear baseline configuration was used. Per baseline, the *H* and *K* band are separated by the HK-discontinuity, but still show a smooth transition between the two.

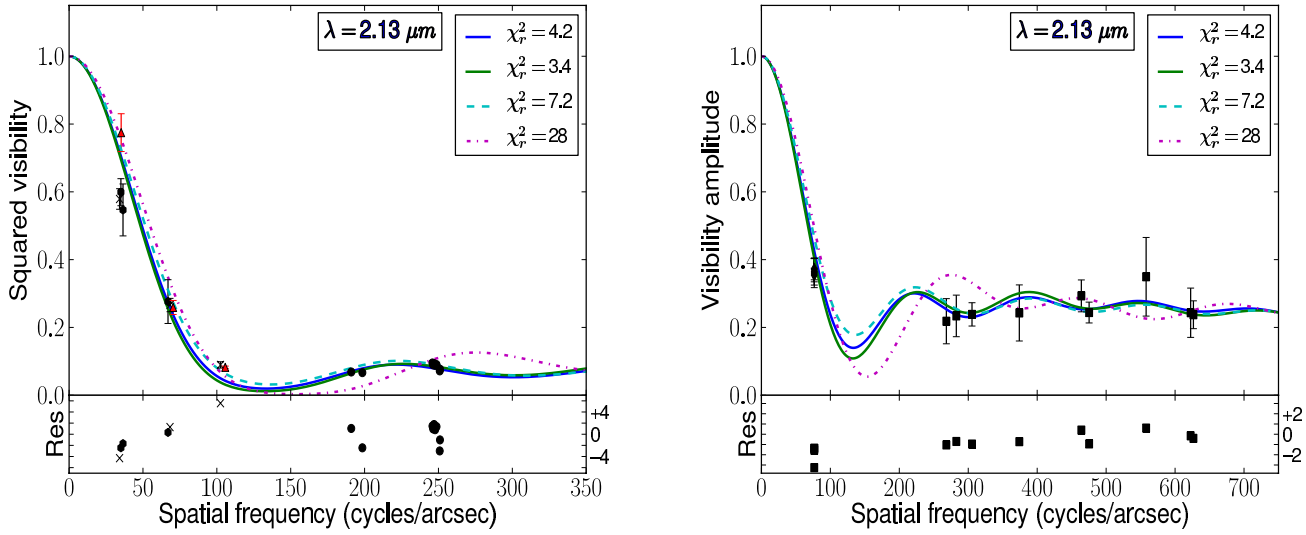

Fig. 4. Same as Fig. 3 but for *K* band (for which there are no IOTA data). The red model is not relevant in *K* and is not shown.

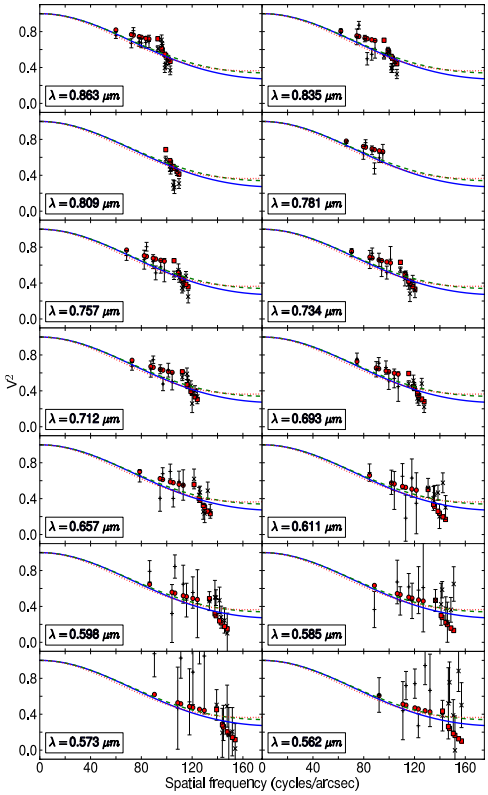

Fig. 6. All NPOI visibilities, except the 673 nm channel which is shown in Fig. 5. A different wavelength is shown in each panel, as indicated. The symbols correspond to different physical baselines, plusses for AC0-AE0 and crosses for AE0-AW0. The blue, green and red lines are the same star+ring models as in Fig. 5, and have ring diameters and widths of (5.5, 1.0), (3.0, 3.0) and (1.0, 4.5) respectively. The red filled circles correspond to the best binary model deduced in Sect. 3.2 and online Fig. 7.

Table 5. Fluxes used in the "stellar SED" fit.

Photometric filter	Total	Stellar	Error
JOHNSON.*V*	5.45[a]	6.00	0.15
JOHNSON.*R*	5.13	5.68	0.12
2MASS.*H*[b]	4.21	4.86	0.11
2MASS.*Ks*[b]	3.41	4.92	0.1
JOHNSON.*H*	4.39	5.04	0.12
JOHNSON.*K*	3.35	4.85	0.12

Notes. For each filter, both the total flux and the stellar flux, i.e. the total flux corrected with the stellar flux fractions of Table 4, are listed. [(a)] Average of AAVSO light curve over 2011–2012; [(b)] Mt. Abu measurements.

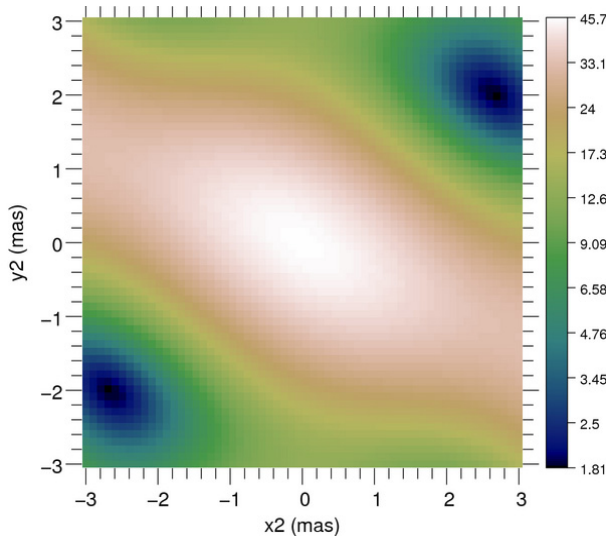

Fig. 7. χ^2_r map of the relative position of the secondary component with respect to the primary at the center, if a binary model is applied to fit the optical NPOI visibilities.

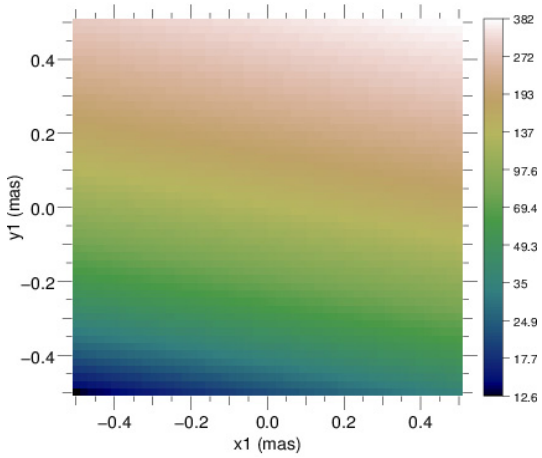

Fig. 9. χ^2_r map of the position x versus y of the post-AGB star with respect to the phase reference defined by the ring (inner diameter 3 mas and width 4.6 mas, see Sect. 3.4).

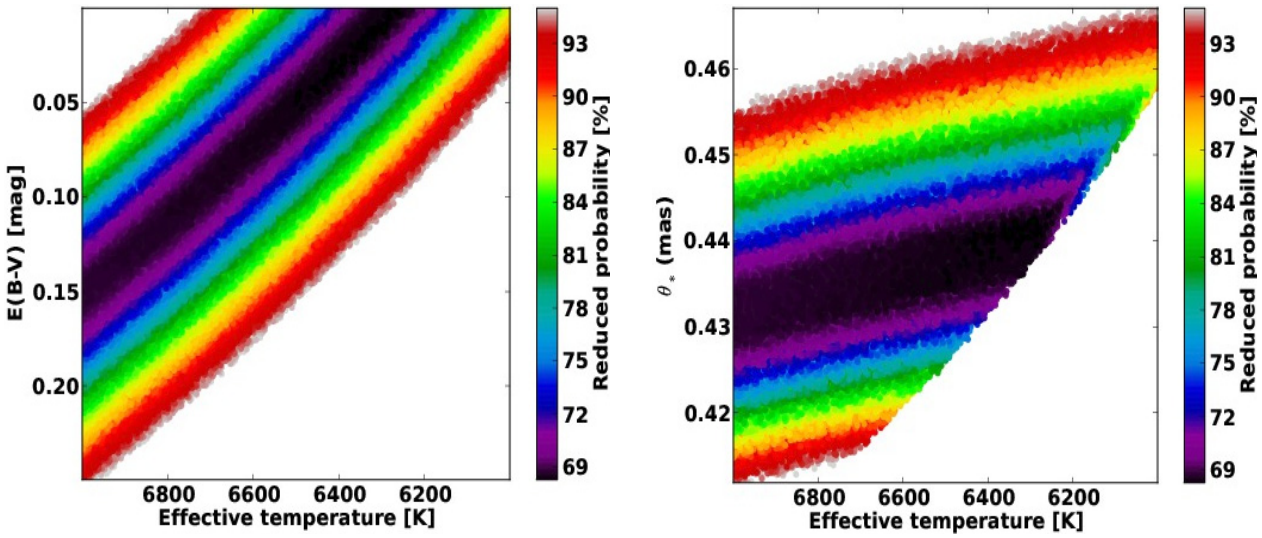

Fig. 10. *Left*: CI of $T_{\rm eff}$ versus $E(B-V)$, *right*: CI of $T_{\rm eff}$ versus angular diameter $\theta_\star$ (mas), for the stellar SED fit.